



Published in final edited form as:

Comput Med Imaging Graph. 2015 April ; 41: 3–13. doi:10.1016/j.compmedimag.2014.11.001.

Selective Invocation of Shape Priors for Deformable Segmentation and Morphologic Classification of Prostate Cancer Tissue Microarrays

Sahirzeeshan Ali^{a,*}, Robert Veltri^b, Jonathan A. Epstein^b, Christhunesa Christudass^b, and Anant Madabhushi^{a,*}

^aDepartment of Biomedical Engineering, Case Western University, Cleveland OH, USA

^bDepartment of Surgical Pathology, The Johns Hopkins Hospital, Baltimore, Maryland, USA

Abstract

Shape based active contours have emerged as a natural solution to overlap resolution. However, most of these shape-based methods are computationally expensive. There are instances in an image where no overlapping objects are present and applying these schemes results in significant computational overhead without any accompanying, additional benefit. In this paper we present a novel adaptive active contour scheme (AdACM) that combines boundary and region based energy terms with a shape prior in a multi level set formulation. To reduce the computational overhead, the shape prior term in the variational formulation is only invoked for those instances in the image where overlaps between objects are identified; these overlaps being identified via a contour concavity detection scheme. By not having to invoke all 3 terms (shape, boundary, region) for segmenting every object in the scene, the computational expense of the integrated active contour model is dramatically reduced, a particularly relevant consideration when multiple objects have to be segmented on very large histopathological images. The AdACM was employed for the task of segmenting nuclei on 80 prostate cancer tissue microarray images from 40 patient studies. Nuclear shape based, architectural and textural features extracted from these segmentations were extracted and found to be able to discriminate different Gleason grade patterns with a classification accuracy of 86% via a quadratic discriminant analysis (QDA) classifier. On average the AdACM model provided 60% savings in computational times compared to a non-optimized hybrid active contour model involving a shape prior.

Keywords

Level set segmentation; Prostate Cancer Detection; Histology; Digital Pathology; Gleason Grading; Shape Prior; Active Contour

© 2014 Elsevier Ltd. All rights reserved.

*Corresponding authors sahirzeeshan.ali@case.edu (Sahirzeeshan Ali), anant.madabhushi@case.edu (Anant Madabhushi).

Publisher's Disclaimer: This is a PDF file of an unedited manuscript that has been accepted for publication. As a service to our customers we are providing this early version of the manuscript. The manuscript will undergo copyediting, typesetting, and review of the resulting proof before it is published in its final citable form. Please note that during the production process errors may be discovered which could affect the content, and all legal disclaimers that apply to the journal pertain.

1. Introduction

Active Contours (AC) can be categorized as boundary-based (first generation) and region-based (second generation) schemes (Kass et al., 1988; Caselles et al., 1997; Chan and Vese, 2001). Most AC models are not intrinsically capable of handling object occlusion or scene clutter. Therefore, the integration of shape priors into the variational formulation represents a natural way to overcome occlusion. Third generation (hybrid) AC models involve combining a shape prior with geometric/geodesic active contours that simultaneously achieves registration and segmentation (Leventon et al., 2000; Rousson and Paragios, 2002; Chan, 2005). Rousson and Paragios (2002) proposed a novel approach for introducing shape priors into level set representations, focused on 2D closed shapes. A limitation of most third generation AC models, however, is that only one pair of overlapping objects can be accurately resolved at a time. Further, most of these methods are sensitive to model initialization and typically require varying degrees of user intervention (Kass et al., 1988; Caselles et al., 1997; Chan and Vese, 2001; Leventon et al., 2000; Rousson and Paragios, 2002; Chan, 2005). Moreover, the efficiency of these hybrid schemes are limited by the computational overhead of the non linearity of the convergence of the evolving curve. Additionally, the shape prior (the most computationally heavy term in the variational formulation) is typically invoked in segmenting every object in the scene, regardless of whether or not an overlap exists. Non-overlapping objects, in most cases, can be segmented by first and second generation AC models alone.

In this paper, a variational adaptive segmentation scheme (AdACM) is presented. The original instantiation of our segmentation method Ali and Madabhushi (2012) combined boundary and region based energy terms with a shape prior in a multi level set formulation to resolve overlapping and non-overlapping nuclei. However, due to the computation overhead of including shape prior energy, such a scheme is computationally expensive for large images (such as histopathology). AdACM selectively invokes the shape prior term in the variational formulation for only those instances in the image where overlaps between objects are identified; these overlaps being identified via a contour concavity detection scheme. By not having to invoke all 3 terms (shape, boundary, region) for segmenting every object in the scene, the computational expense of the integrated active contour model is dramatically reduced, a particularly relevant consideration when multiple objects have to be segmented on very large histopathological images (See Figure 1). Furthermore, most of the shape based level set models reported in literature are only able to handle the overlap resolution of a single pair of objects per image (Leventon et al., 2000; Rousson and Paragios, 2002; Chan, 2005). However, AdACM segmentation scheme provides simultaneous segmentation of all overlapping and non-overlapping objects in very large images.

In their seminal work, Cootes et al. (1995) proposed to use principal component analysis (PCA) to capture the main shape variations of parametric AC's (active shapes) within a training set and thus to represent specific shapes. Consequently, their model is not parametrization free. Leventon et al. (2000) proposed the introduction of prior shape information into AC, intrinsically represented by level set functions, the core idea being to apply PCA on the signed distance functions (SDF) of the parametric ACs. This feature

allowed them to construct an intrinsic and parametrization free shape model. The shape prior is comprised of the mean level set shape and a weighted sum of the m strongest eigen modes of variation (obtained from the PCA of the SDFs). SDFs have the additional advantage that they are more robust to slight misalignments of the training sequence compared to parametric curves. Unfortunately, the shape functions resulting from PCA are not exactly SDFs, as proved by Leventon et al. (2000), but they can nonetheless be used in practice since they are very close to real SDFs. Rousson et al. In a similar fashion, Rousson and Paragios (2002) proposed a method where the optimal weight factors of the eigenmodes of variation are estimated by solving a linear system. Bresson et al. (2003) integrated the geometric shape prior of Leventon et al. (2000) into the segmentation framework based on AC as well as on a region driven term derived from the Chan and Vese energy term (Chan, 2005). In Rousson and Paragios (2002); Paragios and Deriche (1999), the signed distance functions of the training images are computed and the statistics of the signed distance training set is captured via PCA. This representation assumes that the probability distribution function of the training set is Gaussian.

Various segmentation methods have been previously proposed that are bottom-up approaches. Supervised learning (Cheng et al., 2013), multi-reference level-set (Hang Chang et al., 2012), hierarchical partial matching (Petrakis et al., 2002) and various shape-based models (Petrakis et al., 2002; Yang and Jiang, 2001) have been proposed for cell segmentation. Recently, a new non-parametric method was proposed to tackle these three challenges in a unified framework (Zhang et al., 2011a and Zhang et al., 2012). Unlike these previously proposed approaches, our strategy instead of using any parametric model based off shape statistics, incorporates the use of shape priors on-the-fly through a sparse shape composition. However, sparse shape composition has inferior run-time efficiency, in particular when there are a large number of training datasets available for training the model.

Prostate Cancer (Cap) is evidenced by profound histological, nuclear and glandular changes in the organization of the prostate. Grading of surgically removed tumor of CaP is a fundamental determinant of disease biology and prognosis. The Gleason score, the most widespread method of prostate cancer tissue grading used today, is the single most important prognostic factor in Cap strongly influencing therapeutic options (Epstein et al., 1996, 2005). The Gleason score is determined using the glandular and nuclear architecture and morphology within the tumor; the predominant pattern (primary) and the second most common pattern (secondary) are assigned numbers from 1–5. The sum of these 2 grades is referred to as the Gleason score. Scoring based on the 2 most common patterns is an attempt to factor in the considerable heterogeneity within cases of CaP. In addition, this scoring method was found to be superior for predicting disease outcomes compared with using the individual grades alone. Problems with manual Gleason grading include inter-observer and intra-observer variation and these errors can lead to variable prognosis and suboptimal treatment (Veltri et al., 2010). In recent years, computerized image analysis methods have been studied in an effort to overcome the subjectivity of conventional grading system (Madabhushi, 2009; Hipp et al., 2011; Gurcan et al., 2009). An important prerequisite to such a computerized CaP grading scheme, however, is the ability to accurately and efficiently segment histological structures (glands and nuclei) of interest. Previously, texture

based approaches (Jafari-Khouzani and Soltanian-Zadeh, 2003; Huang and Lee, 2009) characterized tissue patch texture via wavlet features and fractal dimension. However, a limitation of these approaches were that the image patches were manually selected to obtain region containing one tissue class on the digitized slide. Doyle et al. (2007) showed that spatial graphs (eg. Voronoi, Delaunay, minimum spanning tree) built using nuclei as vertices in digitized histopathology images, yielded a set of quantitative feature that allowed for improved separation between intermediate Gleason patterns. Farjam et al. (2007) employed gland morphology to identify the malignancy of biopsy tissues, while Diamond, et al. (Diamond et al., 2004) used morphological and texture features to identify 100-by-100 pixel tissue regions as either stroma, epithelium, or cancerous tissue (a three-class problem). Tabesh et al. (2007) developed a CAD system that employs texture, color, and morphometry on tissue microarrays to distinguish between cancer and non-cancer regions, as well as between high and low Gleason grade prostate cancers (both cases used binary classification).

In this work, we leverage the AdACM scheme for automatic segmentation of all nuclei on large digitized tissue microarrays (TMAs) of CaP. Additionally, we leverage the findings of Veltri et al. (2010) who demonstrated a link between nuclear morphology and Gleason grade to develop a nuclear morphology based classifier to predict Gleason grade. We complement the morphologic features extracted from segmented nuclei with (a) graph features extracted from different types of graphs, where the nuclear centers constitute the graph vertices constructed from nuclear centroids and (b) texture features to distinguish primary Grade 3 and Grade 4 prostate cancers. Since the institution of the Epstein criteria (Epstein et al., 2005), there appears to be a trend in pathology grading of prostate tumors towards over-grading, the so called “Gleason drift” whereby most pathologists tend to call prostate cancer patterns starting from 3 and above (corresponding to a score of 6 and above). Consequently, there are almost no prostate cancers that are called 5 and lower, at least in the US. Because of PSA and early detection, more than 80% of the prostate cancers found are therefore a mix of primary grade 3s and 4s (score of 6, 7 and 8) (Epstein et al., 2005), scores of 9 and 10 are rare due to early detection. Since most of the prevalent Gleason scores are 6–8, the patterns that are most important to distinguish between are 3 and 4. Hence, the reason for focusing on only Gleason grades 3 and 4 in this paper. Moreover, grades 3 and 4 have the most variability among pathologists and a good automated Gleason grading scheme needs to be able to accurately and reproducibly distinguish these two patterns. The accuracy of the nuclear classifier is also implicitly reflective of the performance of AdACM, since accurate nuclear segmentation is a pre-requisite for accurately quantifying nuclear morphology. Major contributions of the papers are:

1. Adaptive active contour based on shape prior without user intervention.
2. Selectively invoking shape term (computationally expensive step) in the regions of overlapping nuclei identified by concavity detection, thereby reducing computational complexity.
3. Nuclear morphology based classifier to predict Gleason patterns.

The rest of the paper is structured as follows. Our hybrid active contour method is described in Section 2., while methodologies for selectively invoking energy terms in the active contour model is discussed in Section 3. We discuss feature extraction for Gleason grading

in Section 4, while Section 5 discusses feature selection and classification. We describe the experimental design, results and performance measures in Section 6. In Section 7 we present our concluding remarks.

2. Hybrid Active Contour Model

An image is defined as $\mathcal{C} = (\mathbf{x}, f_g)$ where \mathbf{x} is a 2D grid representing pixels $c \in \mathbf{x}$, with $c = (x, y)$ representing the Cartesian coordinates of a pixel and f_g assigns intensity values to $c \in \mathbf{x}$, where $f_g(c) \in \mathbb{R}$ (gray scale). Table 1 has the description of notations and commonly used symbols in this paper.

The contours that segment the nuclear-boundaries are represented using the level set method, and are evolved by minimizing the variational energy functional. Under the level set framework, the contour is represented implicitly as the zero level of a higher dimensional embedding function, and the contour propagation is performed by evolving the embedding function. This enables handling topological changes of the boundary (splitting and merging) easily.

2.1. Shape Term - F_{shape}

We combine the shape prior, ψ , with a Geodesic Active Contour(GAC) to create the shape functional. The shape prior, ψ , is created using the statistical methods described in (Rousson and Paragios, 2002). Each shape in the training sample is embedded as the zero level set of a higher dimensional surface. The Signed Distance Function (SDF) is used to encode the distance between the level set (shape contour) and the grid pixels. The level set formulation of the shape functional is expressed as:

$$F_{shape} = \int_{\Omega} (\phi(\mathbf{x}) - \psi(\mathbf{x}))^2 |\nabla \phi| \delta(\phi) d\mathbf{x} \quad (1)$$

where $\{\phi\}$ is a level set function, ψ is the shape prior, $\delta(\cdot)$ is the Dirac function, and $\delta(\phi)$ is the contour measure on $\{\phi = 0\}$. Equation 1 introduces a shape prior in such a way that only objects of interest similar to the shape prior can be recovered, and all unfamiliar image structures are suppressed. It evaluates the shape difference between the level set ϕ and the the shape prior ψ at each iteration of the evolution. However, this formulation only solves for a single level set consistent with the shape prior.

2.2. Region Homogeneity Term

We define a functional to drive the shape model towards a homogeneous intensity region using the shape prior. If our objects of interest have a smooth intensity surface, then the Mumford-Shah (MS) model is the most appropriate model to segment these objects (Chan and Vese, 2001). Since the MS method applied on the AC will extract globally homogeneous regions and our objective is to capture an object corresponding to a particular shape space, the best solution is to apply the MS-based force on the shape prior (Chan and Vese, 2001). Indeed, this new force will globally drive the shape prior towards a homogeneous intensity region based on the shape of interest. The functional F_{region} can be

written with the shape function ψ and statistics of partitioned foreground and background regions, u_{in} , u_{out} :

$$F_{region}(\psi, u_{in}, u_{out}) = \int_{\Omega} \Theta_{in} H_{\psi} d\mathbf{x} + \int_{\Omega} \Theta_{out} H_{-\psi} d\mathbf{x}, \quad (2)$$

where ψ is the shape function, H_{ψ} is the Heaviside function (Chan and Vese, 2001), $\Theta_r = |I - u_r|^2 + \mu |\nabla u_r|^2$ and $r \in \{in, out\}$.

2.3. Combining Shape, Boundary and Region-based Functionals

We define a synergistic model to address the problem of object segmentation, integrating a geometric shape prior with local and global intensity information within a variational framework:

$$F = F_1 + F_{region}(\psi, u_{in}, u_{out}), \quad (3)$$

$$F_1 = \beta_1 F_{shape}(C) + \beta_2 F_{boundary}(\phi, \psi), = \int_{\Omega} \beta_1 ((\phi(\mathbf{x}) - \psi(\mathbf{x}))^2) + \beta_2 (g(|\nabla f_g|) |\nabla \phi| \delta(\phi)) d\mathbf{x} \quad (4)$$

where ψ is the shape function of the object of interest given by the PCA (see Section 2.1), g is an edge detecting function, $\delta(\cdot)$ is the Dirac delta function, and $\delta(\phi)$ is the contour measure on $\{\phi = 0\}$, and β_1, β_2 are arbitrary positive constants that balance the contributions of the boundary, shape, and region terms. The proposed functional F_1 is an extension of the work of Chan (2005) where we have integrated a new statistical shape model. Writing out Equation (3) in its entirety we have,

$$F(\Phi, \Psi, u_{in}, u_{out}) = \underbrace{\int_{\Omega} \beta_1 ((\phi(\mathbf{x}) - \psi(\mathbf{x}))^2) + \beta_2 (g(|\nabla f_g|) |\nabla \phi| \delta(\phi)) d\mathbf{x}}_{\text{Shape+boundary force}} + \underbrace{\beta_r \int_{\Omega} \Theta_{in} H_{\psi} d\mathbf{x} + \int_{\Omega} \Theta_{out} H_{-\psi} d\mathbf{x}}_{\text{Region force}} \quad (5)$$

Proof of existence of solution for above model is provided in our previous method (Ali and Madabhushi, 2012).

2.4. Segmenting multiple objects under mutual occlusion

The level set formulation in Equation (5) is limited in that it allows for segmentation of only a single object at a time. In this work, we incorporate the method presented in (Zhang and Pless, 2006) into Equation (5). Consider a given image consisting of multiple objects $\{O_1, O_2, \dots, O_m\}$ of the same shape. For the problems considered in this work (nuclei segmentation on histopathology images), all nuclei are assumed to be roughly elliptical in shape. Instead of partitioning the image domain into mutually exclusive regions, we allow each pixel to be associated with multiple objects or the background. Specifically, we try to find a set of characteristic functions χ_f such that:

$$\chi_f(\mathbf{x}) = \begin{cases} 1 & \text{if } \mathbf{x} \in O_f, \\ 0 & \text{if otherwise.} \end{cases} \quad (6)$$

We associate one level set per object in such a way that any $O_k, O_l, k, l \in \{1, 2, \dots, m\}$ are allowed to overlap with each other within the image. These level set components may both be positive within the area of overlap, and enforce the prior on the shapes of objects extracted from the image. We consider a specific case of segmenting two objects within an input image, which is generalizable to N independent familiar objects.

The simultaneous segmentation of two familiar objects with respect to the given shape prior is solved by minimizing the following modified version of Equation (5):

$$\begin{aligned}
 F(\Phi, \Psi, u_{in}, u_{out}) &= \sum_{a=1}^2 \int_{\Omega} \beta_1 (\phi_a(\mathbf{x}) - \psi(\mathbf{x}))^2 \\
 &+ \beta_2 (g(|\nabla f_g|) |\nabla \phi_a| \delta(\phi_a) d\mathbf{x} \\
 &+ \beta_r \int_{\Omega} (\Theta_{in} H_{\chi_1 \vee \chi_2}) d\mathbf{x} \\
 &+ \int_{\Omega} (\Theta_{out} \\
 &\quad - H_{\chi_1 \vee \chi_2}) d\mathbf{x} \\
 &+ \omega \int_{\Omega} H_{\chi_1 \vee \chi_2} d\mathbf{x} \\
 &+ \sum_{a=1}^2 \int_{\Omega} (\phi_a - \psi_a)^2 d\mathbf{x}.
 \end{aligned} \tag{7}$$

where $H_{\chi_1 \vee \chi_2} = H_{\psi_1} + H_{\psi_2} - H_{\psi_1} H_{\psi_2}$, $H_{\chi_1 \wedge \chi_2} = H_{\psi_1} H_{\psi_2}$, $\Phi = (\phi_1, \phi_2)$, and $\Psi = (\psi_1, \psi_2)$. The fifth term penalizes the overlapping area between the two regions being segmented, and it prevents the two evolving level set functions from becoming identical. Minimizing Equation (7) by alternating with respect to dynamic variables, yields the associated Euler-Lagrange equations, parameterizing the descent direction by time $t > 0$.

General case of $N > 2$. The method described above can be generalized for simultaneous segmentation of $N > 2$ independent objects, all of which can leverage the shape prior ψ_a . Following is the generalized form of Equation 7:

$$\begin{aligned}
& F(\Phi, \Psi, u_{in}, u_{out}) \\
&= \sum_{a=1}^N \int_{\Omega} \beta_1 (\phi_a(\mathbf{x}) - \psi(\mathbf{x}))^2 \\
&+ \beta_2 (g(|\nabla f_g|) |\nabla \phi_a| \delta(\phi_a) d\mathbf{x} \\
&+ \beta_r \int_{\Omega} (\Theta_{in} H_{\chi_1 \vee \chi_2}) d\mathbf{x} \\
&+ \int_{\Omega} (\Theta_{out} \\
&\quad - H_{\chi_1 \vee \chi_2}) d\mathbf{x} \\
&+ \omega \sum_{a \neq b} \int_{\Omega} H_{\chi_1 \vee \chi_2} d\mathbf{x} \\
&+ \sum_{a=1}^N \int_{\Omega} (\phi_a - \psi_a)^2 d\mathbf{x}.
\end{aligned} \tag{8}$$

3. Selectively Invoking Energy terms in Hybrid ACM

3.1. Watershed Based Initialization and Concavity Detection

We use the popular watershed transformation to obtain the initial delineations of nuclear boundaries in the entire image. By creating the binary mask of the delineations, we obtain the estimated boundaries of the nuclei present.

High concavity points are characteristic of contours that enclose multiple objects and represent junctions where object intersection occurs (Figure 2). The area $\mathcal{A}(s)$ of the closed sub-contour s is compared to predetermined area of an ideal nucleus τ_A . Hence a sub-contour is eligible for a split if $\mathcal{A}(s) > \tau_A$. Since $c = (x, y)$, the difference between any two points c_w and c_{w-1} will represent a vector in 2D. Concavity points are detected by computing the angle between vectors defined by three consecutive points $(c_{w-1}, c_w, c_{w+1}) \in s$. The degree of concavity/convexity is proportional to the angle $\theta(c_w)$ as shown in Figure 2. $\theta(c_w)$ can be computed from the dot product relation (Equation 9):

$$\theta(c_w) = \pi - \arccos \left(\frac{(c_w - c_{w-1}) \cdot (c_{w+1} - c_w)}{\|c_w - c_{w-1}\| \|c_{w+1} - c_w\|} \right). \tag{9}$$

A point is considered to be concavity point if $\theta(c_w) > \theta_t$, where θ_t is an empirically set threshold degree. Concavity points can be distinguished from convexity points by computing the cross product of the vectors $(c_w - c_{w-1})$ and $(c_{w+1} - c_w)$, where a concavity point would yield a positive cross product if the point were moving in a counterclockwise direction on s (see Fig. 2). The value of $\theta(c_w)$ for an eligible concavity point c_w is constrained to be less than an empirically determined value θ_{max} . The value of θ_{max} serves as a threshold for detecting meaningful concavity points and in our case it was found that

$\theta_{max} = \frac{8}{9}\pi$ yielded optimal results. Note that numerous false concavity points may also be detected due to noisy boundaries on the contour.

3.2. Adaptive Selection of Energy Functionals in Hybrid AC Model

The number of detected concavity points, $c_c - 1$, indicates presence of a single non overlapping nucleus. In such cases, shape prior constraint is not necessary and we reduce the model to only employ the region term by setting $\beta_1 = 0$. Similarly, l number of c_c indicate the presence of l overlapping objects. Hence in those regions we initialize the model with the integrated hybrid model (region, boundary, shape terms) with l level sets and set $N = l$ (in Equation 7). The initial contour (as defined by watershed segmentation) is defined as a circle of radius r at the center of the contour, which is also serves as the seed point for placement of the initial level set. Figure 3 illustrates the work flow from initialization to final segmentation for AdACM.

4. Feature Extraction for Discriminating Gleason Patterns

We seek to develop a feature set that describes the nuclear morphological, architectural, and textural attributes of CaP from tissue microarrays are then used to describe and discriminate between the different Gleason patterns in the TMAs.

From each image \mathcal{C} a feature vector F is created comprising the nuclear, graph, and textural based attributes. These values are calculated as described below.

4.1. Nuclear Morphology

A total of 7 nuclear features from each of the segmented nuclei were extracted. These nuclear morphologic features include: Area Overlap Ratio, Average Radial Ratio, Compactness, Convexity, Mean Nuclear Area, Mean Nuclear Perimeter, Mean Nuclear Diameter.

4.2. Nuclear Architecture

We calculate features that describe the spatial location of nuclei within the histological image. On each of the segmented nuclei, center of mass is calculated to represent the nuclear centroid. To analyze the nuclear architecture in greater detail, we construct a series of graphs, using the nuclear centroids as nodes of the graph. Quantifiable features are then extracted from the these graphs (see Table 2).

We denote a graph as $\mathcal{G} = (V, E, W)$, where V are vertices, E are edges, and W are edge weights, proportional to length. The set of vertices, edges, and weights make up a unique graph on \mathcal{R} . We construct the following graphs (illustrations are shown in Figure 4)

Voronoi Diagram (\mathcal{G}_V)—The Voronoi Diagram partitions \mathcal{R} into a set of polygons with centroids V , where a non-centroid pixel is assigned to the polygon of the closest centroid pixel. This yields a tessellation of the image, as shown in Figure 4(b). Pixels that are equidistant from exactly two centroids make up E (edges of the graph), while pixels equidistant from three or more centroids make up the intersections of multiple edges. The perimeter, area, and chord lengths of each polygon in \mathcal{G}_V are computed, and the average, standard deviation, disorder, and minimum to maximum ratio of each are calculated for a total of 12 Voronoi-based features per \mathcal{C} .

Delaunay Triangulation (\mathcal{G}_D)—The Delaunay Triangulation is a triangulation of vertices V such that the circumcircle of each triangle contains no other vertices. The Delaunay and Voronoi graphs are dual to each other, meaning that two points are connected in \mathcal{G}_D if and only if their polygons in \mathcal{G}_V share an edge. An example of \mathcal{G}_D is given in Figure 4(c). From this graph, we compute the area and perimeter of each triangle, and the average, standard deviation, disorder, and minimum to maximum ratio of these are calculated to yield 8 Delaunay-based features per \mathcal{C} .

Minimum Spanning Tree (\mathcal{G}_M)—A spanning tree of a set of points V is an undirected, fully connected graph on V . The weight W of the graph is the sum total of all edges E , and the Minimum Spanning Tree (MST) is the spanning tree with the lowest overall W . The MST, denoted \mathcal{G}_M , is a subgraph of the Delaunay Triangulation. An example of \mathcal{G}_M is given in Figure 4(d). We calculate the average, standard deviation, disorder, and minimum to maximum ratio of the weights W to yield 4 MST-based features per \mathcal{C} .

4.3. Tissue Texture Feature Extraction

The proliferation of nuclei, difference in size and shape leads to a change in overall textural characteristics in a region of interest (ROI). To quantify this change in tissue texture characteristics, we calculate a number of low-level image statistics from each ROI. These statistics can be broadly characterized into two groups: first-order statistics, second-order co-occurrence features. Each of these is calculated in a pixel-wise fashion and are computed independently for each of the hue, saturation, and intensity channels of the original scanned image, generating a set of corresponding feature images. The average, standard deviation, and mode of each of these feature images is calculated, yielding a texture feature vector to quantify the image. In total, 253 texture features are calculated in this manner. The details of each feature type are given below.

First-order Statistics—We calculate 15 different first-order statistics from each image, including average, median, standard deviation, and range of the image intensities within the sliding neighborhood, as well as the Sobel filters in the vertical, horizontal, and both diagonal axes, 3 Kirsch filter features, gradients in the vertical and horizontal axes, difference of gradients, and diagonal derivative. By calculating these 15 features for each channel in the image, and then calculating the mean, standard deviation, and mode of the feature images, we obtain a total of 135 first-order statistics for \mathcal{C} .

Co-occurrence Features—Co-occurrence features, also referred to as Haralick features (Haralick et al., 1973), are computed by constructing a symmetric 256×256 co-occurrence matrix which describes the frequency with which two different pixel intensities appear together within a fixed neighborhood. The number of rows and columns in the matrix are determined by the maximum possible value in a channel of \mathcal{C} ; for 8-bit images, this corresponds to $2^8 = 256$. Element (a, b) in the matrix is equal to the number of times pixel value a occurs adjacent to pixel value b in \mathcal{C} . From the co-occurrence matrix, a set of 13 Haralick features are calculated: contrast energy, contrast inverse moment, contrast average, contrast variance, contrast entropy, intensity average, intensity variance, intensity entropy, energy, correlation, entropy, and two measures of information. Extracting these values from

each channel and taking the mean, standard deviation, and mode of each feature image yields a total of 117 co-occurrence features.

5. Feature Selection and Classification

5.1. Minimum Redundancy Maximum Relevance Scheme

There are many potential benefits of variable and feature selection: facilitating data visualization and data understanding, reducing the measurement and storage requirements, reducing training and utilization times, defying the curse of dimensionality to improve prediction performance. After extracting texture features, we utilized the minimum Redundancy Maximum Relevance (mRMR) feature selection scheme (Peng et al., 2005) in order to identify an ensemble of features that will allow for optimal classification of CaP primary grade 3 versus 4. The feature selection scheme is used to identify the most discriminatory attributes from among all of the textural, architectural, and nuclear morphologic features extracted.

In the following description, the selected subset of features \mathbf{Q} is comprised of feature vectors $F_i, i \in \{1, \dots, |\mathbf{Q}|\}$ (note that $\mathbf{F} = \{F_1, \dots, F_N\}$, $\mathbf{Q} \subset \mathbf{F}$ and $|\mathbf{Q}| < N$). The mRMR scheme attempts to simultaneously optimize two distinct criteria. The first is "maximum relevance" which selects features F_i that have the maximal mutual information (MI) with respect to the corresponding label vector L . This is expressed as

$$U = \frac{1}{|\mathbf{Q}|} \sum_{F_i \in \mathbf{Q}} MI(F_i, L) \quad (10)$$

The second is "minimum redundancy" which ensures that selected features $F_i, F_j \in \mathbf{Q}, i, j \in \{1, \dots, |\mathbf{Q}|\}$, are those which have the minimum MI with respect to each other, given as

$$V = \frac{1}{|\mathbf{Q}|^2} \sum_{F_i, F_j \in \mathbf{Q}} MI(F_i, F_j) \quad (11)$$

Under the second constraint, the selected features will be maximally dissimilar with respect to each other, while under the first, the feature selection will be directed by the similarity with respect to the class labels. There are two major variants of the mRMR scheme: the MI difference (MID, given by $U - V$) and the MI quotient (MIQ, given by U/V). These variants represent different techniques to optimize the conditions associated with mRMR feature selection. In this study, we evaluated the use of both MID and MIQ for feature selection as well as determined an optimal number of features by varying $|\mathbf{Q}|$ the mRMR algorithm.

5.2. Quadratic Discriminant Analysis

The Quadratic Discriminant Analysis (QDA) classifier aims to find a transformation of the input features that is able to optimally discriminate between the classes in the dataset. Given a set of samples C with associated feature set, \mathbf{F} , QDA solves for $\mathbf{Y} = \mathbf{F}^T \mathbf{A} \mathbf{F} + \mathbf{B}^T \mathbf{F}$, where $\mathbf{Y} = \{Y_1, Y_2, \dots\}$ denotes the resultant vector of QDA.

Based on calculating the means $\mu_{l(C)=+1}$, $\mu_{l(C)=-1}$ and covariances $\Sigma_{l(C)=+1}$, $\Sigma_{l(C)=-1}$ of the 2 classes in the dataset (Grade 3 and Grade 4), we can solve the equation below to calculate the following log likelihood ratio:

$$\log(\mathbf{H}) = \frac{(\mathbf{F} - \mu_{l(C)=+1})^T \Sigma_{l(C)=+1}^{-1} (\mathbf{F} - \mu_{l(C)=+1})}{(\mathbf{F} - \mu_{l(C)=-1})^T \Sigma_{l(C)=-1}^{-1} (\mathbf{F} - \mu_{l(C)=-1})}. \quad (12)$$

6. Experimental Design and Performance Measures

6.1. Data Description

Our dataset comprised a total of 80 images obtained from 40 patient cases, in the form of TMAs with 2 TMAs per patient study. The various CaP tissues and controls included in these TMAs were selected and reviewed by a John Hopkins Hospital pathologist. Slides from all cases selected are reviewed and mapped by a pathologist and the normal-appearing and staged and/or graded index tumor areas were identified and marked on the slide for each case. Using these template slides marked for normal-appearing (adjacent) and diagnostic CaP areas, the tissue blocks were coordinately marked using the template slides, and 0.60-mm cores were punched from the normal-appearing and CaP areas and then transferred to recipient blocks. The TMAs were prepared (both normal-appearing and cancer areas) using a Beecher MT1 manual arrayer (Beecher Instruments, Silver Spring, MD) in the Johns Hopkins Hospital TMAJ pathology core facility. Each TMA was constructed using four replicate 0.6mm core tissue samples from the normal-appearing and cancer areas of each patient who had undergone radical prostatectomy for CaP. The 40 studies (consisting of TMAs for cancer areas) comprised 13 Gleason patterns 6 (3+3), 8 pattern 7 (3+4), 7 (4+3) pattern 7, 7 pattern 8 (4+4) and 5 pattern 9 (4+5) studies where the first number in the parenthesis refers to the primary and the second number to the secondary Gleason grade.

6.2. Comparative Strategies

We qualitatively and quantitatively compared the segmentation performance with the GAC (Geodesic Active Contour) (Caselles et al., 1997) and the Rousson shape based model (RD) (Rousson and Paragios, 2002). The RD model is a popular region based AC model where the model is driven by the Gaussian distribution of both foreground and background and also involves a shape prior.

Experiment 1 Overlap Resolution: The aim of this experiment was to demonstrate the ability of our scheme to correctly resolve the overlap between all intersecting nuclei across 80 histopathology images.

Experiment 2 Comparison of our model against the GAC and Rousson-Derich (RD) models in terms of detection accuracy: The aim of this experiment was to compare the detection accuracy of our model over two state-of-the-art AC models, GAC and RD.

Experiment 3 Comparison against GAC and RD model in terms of segmentation accuracy: The aim of this experiment was to compare the segmentation performance in terms of boundary and area overlap metrics compared to the GC and RD model.

Experiment 4 Runtime analysis and computational efficiency: The aim of this experiment was to evaluate the computational efficiency and speed up achieved by AdACM compared against other models.

Experiment 5 Classifier Accuracy: The aim of this experiment is to evaluate classifier accuracy in distinguishing grade 3 vs grade 4. Furthermore, we evaluate the optimal feature set determined by mRMR feature selection method.

6.3. Performance Measures

6.3.1. Evaluation of Detection Performance—The metrics used to evaluate object detection include: 1) sensitivity (SN); 2) positive predictive value (PPV); and 3) overlap detection ratio (OR) (see Table 3). The detection results from three models (Chan-Vese, our model and RD) are compared to manual detection results obtained from an expert clinician. The SN and PPV values are computed from the true-positive (TP), false-positive (FP), and false negative (FN) values (TP, FN, FP are subsequently defined):

$$SN = \frac{TP}{TP + FN}, \quad (13)$$

$$PPV = \frac{TP}{TP + FP}. \quad (14)$$

TP refers to the number of nuclei correctly identified while FP refers to the number of objects incorrectly identified as lymphocyte nuclei and FN refers to the number of nuclei missed by the model. The detection results are represented as the centroid of the region enclosed by a closed contour. TP, FP, and FN values are obtained by comparing each centroid generated by the model to manually determined object centroid. The overlap detection ratio (OR) (Table 2) is computed as follows:

$$OR = \frac{\text{Number of overlaps resolved}}{\text{Total Number of overlaps}}.$$

An overlap is characterized by the existence of a common boundary between two objects and in our case may be between two or more nuclei.

6.3.2. Evaluation of Segmentation Performance—Segmentation results are compared to manual delineations performed by an expert oncologist (which serves as ground truth for segmentation evaluation) by computing boundary based metrics, namely Hausdorff distance (HD), mean absolute distance (MAD), and area overlap metrics (true positive area (TP_a), false-positive area (FP_a), true-negative area (TN_a), and false-negative area (FN_a)). The manual delineation is represented as a closed boundary \mathcal{G} .

For each of the 8040 nuclear boundary segmentations, a corresponding value for HD and MAD were obtained. HD and MAD values close to zero correspond to better segmentation. The area overlap metrics are used to compute the sensitivity SN_a , specificity SP_a , positive

predictive value PPV_a and the overlap ratio OV_a of the segmentation results for each of the three models. The area overlap metrics are computed as follows:

$$TP_a = \frac{|\mathcal{A}(S) \cap \mathcal{A}(\mathcal{G})|}{A(\mathcal{G})}, \quad FP_a = \frac{|\mathcal{A}(S) \cup \mathcal{A}(\mathcal{G}) - \mathcal{A}(\mathcal{G})|}{A(\mathcal{G})}, \quad FN_a = \frac{|\mathcal{A}(S) \cup \mathcal{A}(\mathcal{G}) - \mathcal{A}(S)|}{A(\mathcal{G})}, \quad \text{and } TN_a = \frac{|C - \mathcal{A}(\mathcal{G})|}{A(\mathcal{G})}.$$

where $\mathcal{A}(\cdot)$ is the area of the closed boundary. For each image, the set of pixels lying within the manual delineations of the nuclei is denoted as $\mathcal{A}(\mathcal{G})$. $\mathcal{A}(S)$ is the set of pixels whose level set functions are positive, after the convergence of active contour model. The SN_a and PPV_a values are computed in a similar fashion as described in (13) and (14), respectively. SP_a and OV_a values are computed as follows:

$$SP_a = \frac{TN_a}{TN_a + FP_a}, \quad OV_a = \frac{TP_a}{TP_a + FP_a + FN_a}.$$

7. Results and Discussion

7.1. Qualitative Results

Qualitative results for 3 studies illustrated in Figure 5 reflect the superiority of our model in resolving overlapping nuclei. For the CaP TMA images (1024×1024), we applied AdACM for nuclear segmentation.

7.2. Quantitative Results

Results of quantitative evaluation of detection and segmentation performance for each of the three models are shown in Tables 3 and 4. These results reflect the improved performance over Rousson and GAC, respectively. The SN and PPV values listed in Table 3 reflect the efficacy of our model in detecting nuclei in prostate images as compared to other two models.

In terms of segmentation performance, our model easily outperformed both Rousson and GAC models, respectively, in terms of all six segmentation evaluation measures over 8040 nuclei from 80 images. The HD and MAD values for our model were less than 5 pixels for over 95% of the studies respectively. The statistical measures from the area overlap metrics are summarized in Table 4

7.3. Runtime Analysis and Computational Efficiency

We evaluated the computational efficiency of AdACM with respect to a hybrid ACM (HACM) which did not employ selective invocation of the shape prior. On 100 image patches of 200×200 pixels and in the presence of average of 114 nuclei with 40 overlaps per patch, AdACM required 252s to accurately segment nuclei and resolve all intersections, compared to HACM which took 560s; all evaluations being performed on a 3 GHz, dual core processor with 4 GB RAM. Table 5 summarizes runtime for individual modules of the AdACM algorithm. It can be noted that majority of the time (70%) is spent in energy evolution and thus selective invocation of shape prior reduces evolution complexity thereby reduction complexity of the entire method.

7.4. Evaluating Discriminability of Feature Classes

The extracted features are aggregated into feature set $\mathcal{Q}^{\text{Tot}} = \{\mathcal{Q}^{\text{Arc}}, \mathcal{Q}^{\text{Tex}}, \mathcal{Q}^{\text{Nuc}}\}$, where $\mathcal{Q}^{\text{Arc}}, \mathcal{Q}^{\text{Tex}}, \mathcal{Q}^{\text{Nuc}}$ refer to architectural, textural and nuclear features. 3D features plots in Figure 6 illustrate each feature set's ability in separating Gleason grade 3 vs grade 4. Note that the features plots in Figures 6 (a) suggest that the nuclear shape features are able to capture the subtle morphologic differences between the two Gleason patterns, in turn reflecting the accuracy of AdACM.

7.5. Classification Accuracy

We employed mRMR algorithm to prune \mathcal{Q}^{Tot} to provide an optimal number of features that can be used to train the QDA classifier to accurately distinguish between intermediate primary grade 3 and grade 4 tumors. The main free parameter associated with the mRMR scheme is the number of features to be selected ($|\mathcal{Q}|$). We empirically varied the number of features and evaluated the classification for each resulting feature set using a QDA classifier. We found that an ensemble of 28 features as determined via from mRMR was the optimal feature set size (top 10 of the 28 features are listed in Table 6). Figure 6(d) illustrates a clear separation of Grade 3 and Grade 4 with the feature set found by mRMR. Figure 7 illustrates the effect of varying the size of the feature ensemble as a function of classification accuracy.

For a database of 80 images, the QDA classifier achieved an accuracy of $86.1 \pm 0.5\%$ in distinguishing primary grade 3 from 4 using an ensemble of 28 features chosen from across all the 3 feature classes. In order to ensure robustness of the feature selection and classifier, a randomized 3 fold cross-validation procedure was implemented. In a single cross-validation run, the dataset is divided into 3 randomized subsets (comprising 27, 27 and 26 images). Two subsets were considered as training data and the remaining as testing data, following which classification is performed. This was repeated until all 3 subsets were classified, and the entire cross-validation procedure was iterated 10 times. QDA classification accuracies and the pruned number of features are given in Table 8.

8. Concluding Remarks

In this work we presented a new hybrid active contour that employs a shape prior for concurrent segmentation of multiple overlapping nuclei. Our model (AdACM) selectively invokes the shape prior terms (the most computationally expensive step of the hybrid active contour model) in those image regions where objects overlap, overlaps being determined via a concavity detection scheme. This selective invocation of energy terms in the variational formulation yields a hybrid ACM that is both accurate and computationally efficient. We extracted nuclear, architectural and texture based features to automatically distinguish the primary, intermediate Gleason grades of prostate cancer tissue microarrays. Morphologic features derived from nuclei segmented via AdACM yielded the highest accuracy amongst all the feature categories considered (architectural, nuclear, textural) in discrimination of intermediate Gleason grade patterns (3 versus 4), on prostate cancer TMAs, in turn reflecting the segmentation accuracy of AdACM. By employing Minimum Redundancy Maximum Relevance feature selection Scheme, we were able to select an optimal number of

features spanning the architectural, morphologic, and textural attribute classes to train a Quadratic Discriminant Analysis classifier. The combination of the best features across all the feature classes (nuclear, architectural, and textural) yielded a higher classification accuracy compared to any of the individual feature categories.

In this study we limited ourselves to only attempting to distinguish between primary Gleason grades 3 and 4. Due to the relatively small size of the dataset we did not attempt to train the classifier to distinguish the prostate cancer TMAs based off Gleason scores. Preliminary qualitative results derived from the PCA embeddings of the nuclear morphologic features suggest that our combined segmentation and classification scheme does appear to separate out the TMAs based off their Gleason scores. In future work, we intend to increase the size of our dataset in order to be able to train and evaluate the classifier presented in this paper to automatically separate out Gleason scores. Additionally we also intend to leverage AdACM in the context of nuclear and cell segmentation in other domains within digital pathology.

Acknowledgment

National Institutes of Health under award numbers R01CA136535- 01, R01CA140772-01, and R21CA167811-01; the National Institute of Diabetes and Digestive and Kidney Diseases under award number R01DK098503-02, the DOD Prostate Cancer Synergistic Idea Development Award (PC120857); the QED award from the University City Science Center and Rutgers University, the Ohio Third Frontier Technology development Grant. The content is solely the responsibility of the authors and does not necessarily represent the official views of the National Institutes of Health.

References

- Ali S, Madabhushi A. An integrated region, boundary, shape based active contour for multiple object overlap resolution in histological imagery. *IEEE Trans on Medical Imaging*. 2012;100–114.
- Bresson X, Vanderghelynst P, Thiran J. A priori information in image segmentation: energy functional based on shape statistical model and image information. *IEEE Int. Conf. on Image Processing*. 2003; 3:425–438.
- Caselles V, Kimmel R, Sapiro G. Geodesic active contours. *International Journal of Computer Vision*. 1997; 22(1):61–79.
- Chan, T. *EEE Computer Society Conference on Computer Vision and Pattern Recognition*. Springer; 2005. Level set based shape prior segmentation; p. 164–1170.
- Chan T, Vese L. Active contours without edges. *IEEE TIP*. 2001 Feb; 10(2):266–277.
- Cheng, C.; Wang, W.; Ozolek, J.; Rohde, G. Cytometry. *PMC*; 2013. A flexible and robust approach for segmenting cell nuclei from 2d microscopy images using supervised learning and template matching; p. 495507
- Cootes T, Cooper D, Taylor C, Graham J. Active shape models - their training and application. *Computer Vision and Image Understanding*. 1995; 61:38–59.
- Diamond J, Anderson N, Bartels P, Montironi R, Hamilton P. The use of morphological characteristics and texture analysis in the identification of tissue composition in prostatic neoplasia. *Human Pathology*. 2004; 35(9):1121–1131. [PubMed: 15343515]
- Doyle S, Hwang M, Shah K, Madabhushi A, Tomasezewski J, Feldman M. Automated grading of prostate cancer using architectural and textural image features. *International Symposium on Biomedical Imaging (ISBI)*. 2007; 28:1284–1287.
- Epstein J, Allsbrook W, Amin M, Egevad L. The 2005 international society of urological pathology (isup) consensus conference on gleason grading of prostatic carcinoma. *American Journal of Surgical Pathology*. 2005; 29(9):1228–1242. [PubMed: 16096414]

- Epstein J, Walsh P, Sanfilippo F. Clinical and cost impact of second-opinion pathology. review of prostate biopsies prior to radical prostatectomy. *American Journal of Surgical Pathology*. 1996; 20(7):851857.
- Farjam R, Soltanian-Zadeh H, Jafari-Khouzani K, Zoroofi R. An image analysis approach for automatic malignancy determination of prostate pathological images. *Cytometry Part B (Clinical Cytometry)*. 2007; 72(B):227–240.
- Fatakdwala H, Xu J, Basavanthally A, Bhanot G, Ganesan S, Feldman M, Tomaszewski J, Madabhushi A. Em driven geodesic active contour with overlap resolution (emagacor): Application to breast cancer histopathology. In: *IEEE TBE*. 2010 Jun.:69–76.
- Gurcan M, Boucheron L, Can A, Madabhushi A, Rajpoot N, Yener B. Histopathological image analysis: A review. *IEEE Reviews in Biomedical Engineering*. 2009; 2:147–171. [PubMed: 20671804]
- Hang Chang, H.; Paul, S.; Parvin, B. *IEEE Trans Biomed Eng*. PMC; 2012. Multireference level set for the characterization of nuclear morphology in glioblastoma multiforme; p. 34603467
- Haralick R, Shanmugam K, Dinstein I. Textural features for image classification. *Systems, Man and Cybernetics, IEEE Transactions on SMC-3*. 1973; (6):610–621.
- Hipp J, Flotte T, Monaco J, Cheng J, Madabhushi A, Yagi Y, Rodriguez-Canales J, Emmert-Buck M, Dugan M, Hewitt S, Toner M, Tompkins R, Lucas D, Gilbertson J, Balis U. Computer aided diagnostic tools aim to empower rather than replace pathologists: Lessons learned from computational chess. *Journal of Pathology Informatics*. 2011; 2(1):25–28. [PubMed: 21773056]
- Huang P, Lee C. Automatic classification for pathological. prostate images based on fractal analysis. *Medical Imaging, IEEE Transactions on*. 2009; 28:1037–1050.
- Jafari-Khouzani K, Soltanian-Zadeh H. Multiwavelet grading of pathological images of prostate. *Biomedical Engineering, IEEE Transactions on*. 2003; 50:697–704.
- Kass M, Witkin A, Terzopoulos D. Snakes: Active contour models. *IJCV*. 1988; 1(4):321–331.
- Leventon M, Grimson WEL, Faugeras O. Statistical shape influence in geodesic active contours. *Computer Vision and Pattern Recognition, 2000. Proceedings. IEEE Conference on*. 2000; 1:316–323. vol.1.
- Madabhushi A. Digital pathology image analysis: Opportunities and challenges (editorial). *Imaging in Medicine*. 2009; 1(1):7–10.
- Paragios N, Deriche R. Unifying boundary and region-based information for geodesic active tracking. *CVPR*. 1999; 2:305. Vol. 2.
- Peng H, Long F, Ding C. Feature selection based on mutual information criteria of max-dependency, max-relevance, and min-redundancy. *Pattern Analysis and Machine Intelligence, IEEE Transactions on*. 2005; 27(8):1226–1238.
- Petrakis, E.; Diplaros, A.; Milios, E. *Pattern Analysis and Machine Intelligence, IEEE Transactions on*. IEEE; 2002. Matching and retrieval of distorted and occluded shapes using dynamic programming; p. 1501-1516.
- Rousson, M.; Paragios, N. *ECCV*. Springer; 2002. Shape priors for level set representations; p. 78-92.
- Tabesh A, Teverovskiy M, Pang H, Verbel VKD, Kotsianti A, Saidi O. Multi feature prostate cancer diagnosis and gleason grading of histological images. *IEEE Transactions on Medical Imaging*. 2007; 26(10):1366–1378. [PubMed: 17948727]
- Veltri R, Isharwal S, Mille M. Nuclear roundness variance predicts prostate cancer progression, metastasis, and death: A prospective evaluation with up to 25 years of follow-up after radical prostatectomy. *The Prostate*. 2010; 70:1330–1339.
- Yang, F.; Jiang, T. *Journal of Biomedical Informatics. IEEE*; 2001. Cell image segmentation with kernel-based dynamic clustering and an ellipsoidal cell shape model; p. 67-73.
- Zhang Q, Pless R. Segmenting multiple familiar objects under mutual occlusion. *ICIP*. 2006

Highlights

This work presents an optimized region, boundary and shape based multi-level set segmentation scheme, which selectively leverages shape prior energy functional to resolve overlap and non-overlapping objects. We leverage this new segmentation scheme to develop a CAD system to perform automated Gleason grading on large histopathology images.

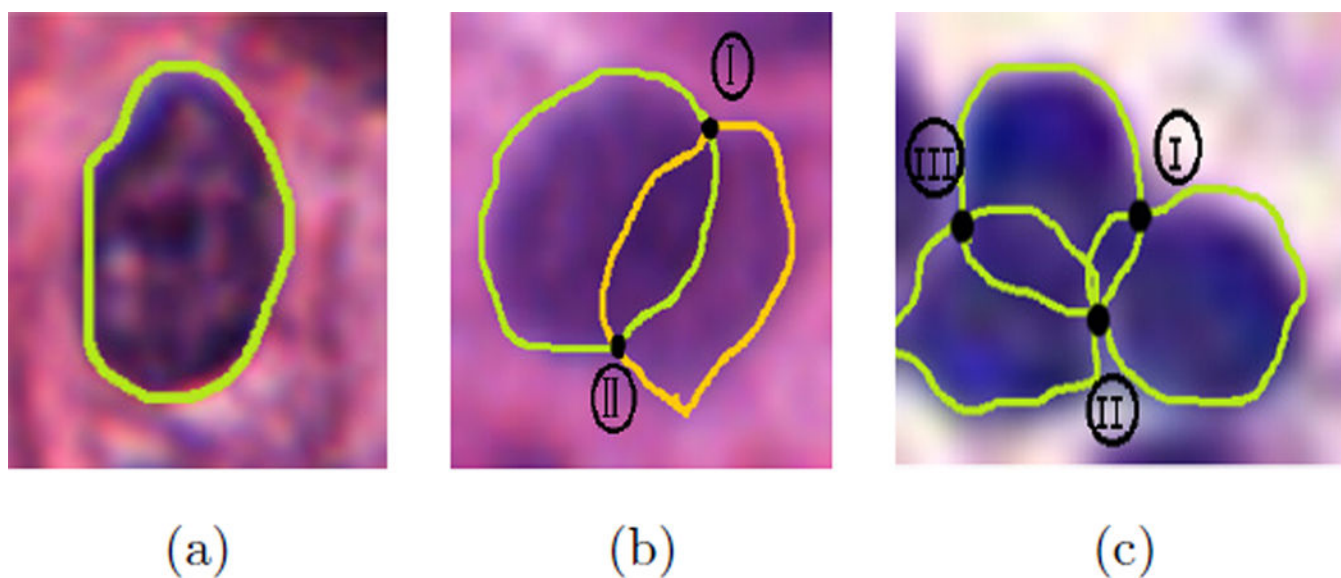


Figure 1. Selective incorporation of variational terms based on detection of concavity points (representative of overlapping objects). In (a) the absence of concavity point reflects the presence of a single nucleus. Similarly (b) and (c) detection of the number of concavity points represents the number of nuclei.

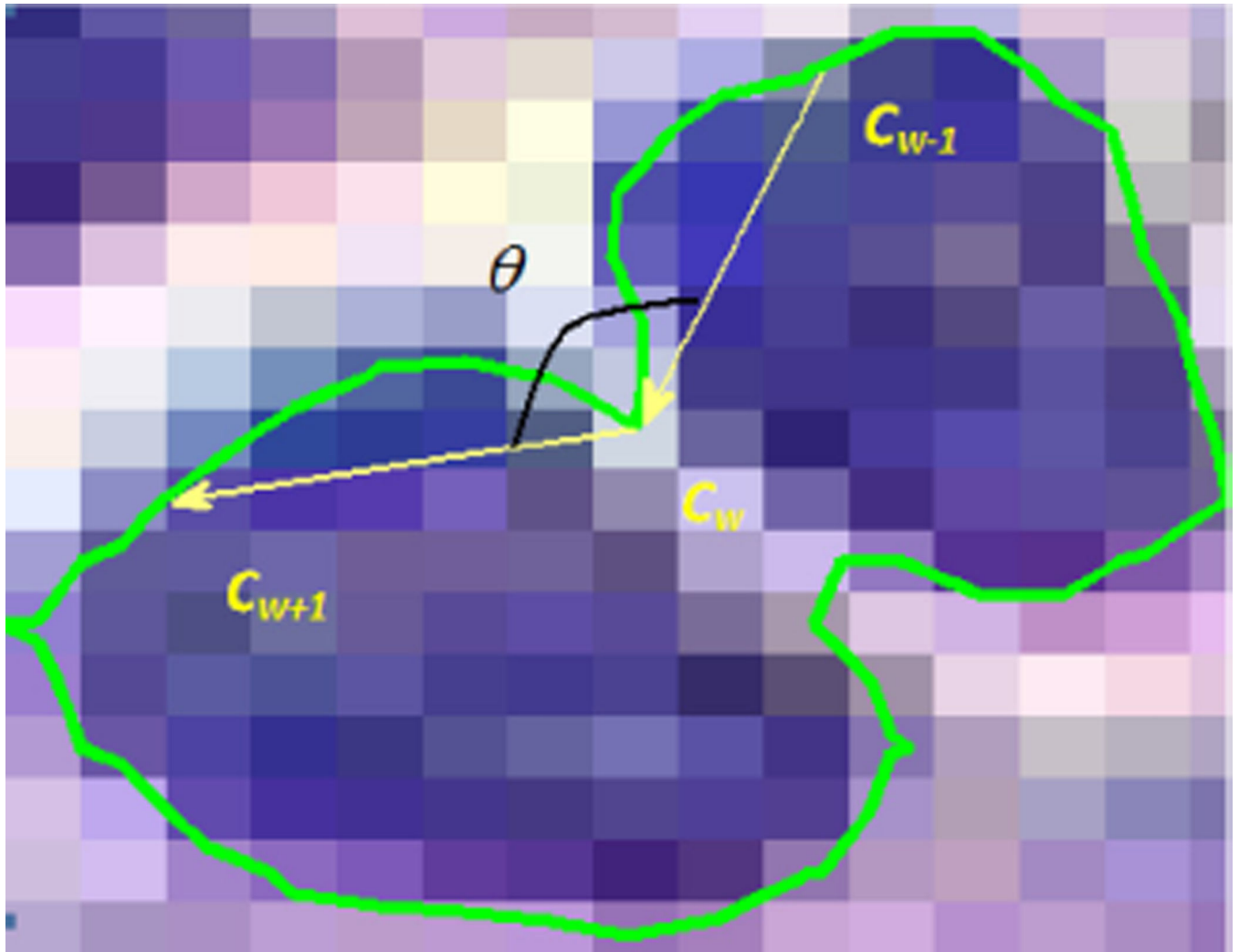


Figure 2. Concavity detection: Three consecutive points on s (c_{w-1} , c_w and c_{w+1}) are used to define two vectors (shown with arrows). The angle θ between them is a measure of concavity/convexity of the point c_w (Fatakda et al., 2010).

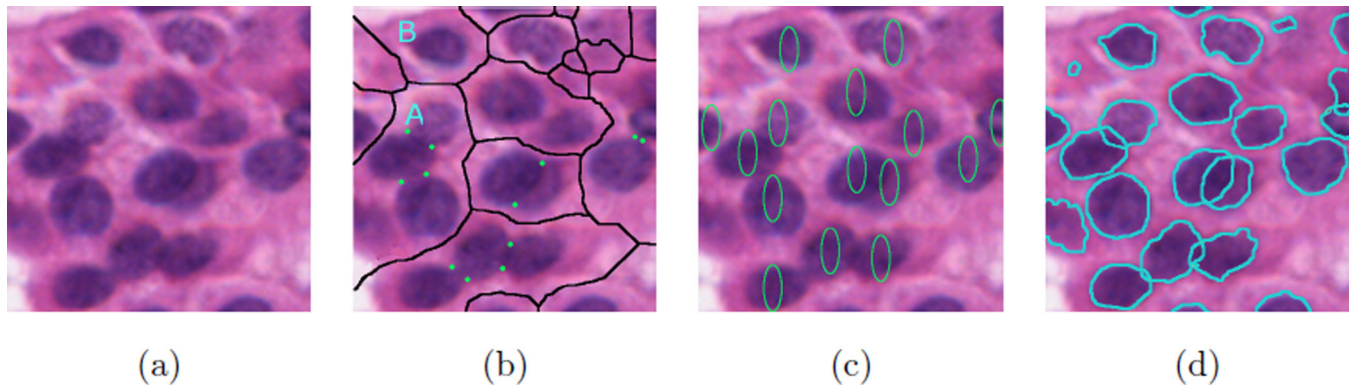


Figure 3.

Constituent modules of the AdACM. (a) Original image; (b) Watershed segmentation of individual nuclei with an overlay detected concavity points; (c) Placement of initial level sets in the image; (d) final segmentation. Note that in the region shown as A where 4 concavity points were detected, 3 level sets were initialized with the shape prior, whereas in region B, only a single level set (only region based term) was initialized.

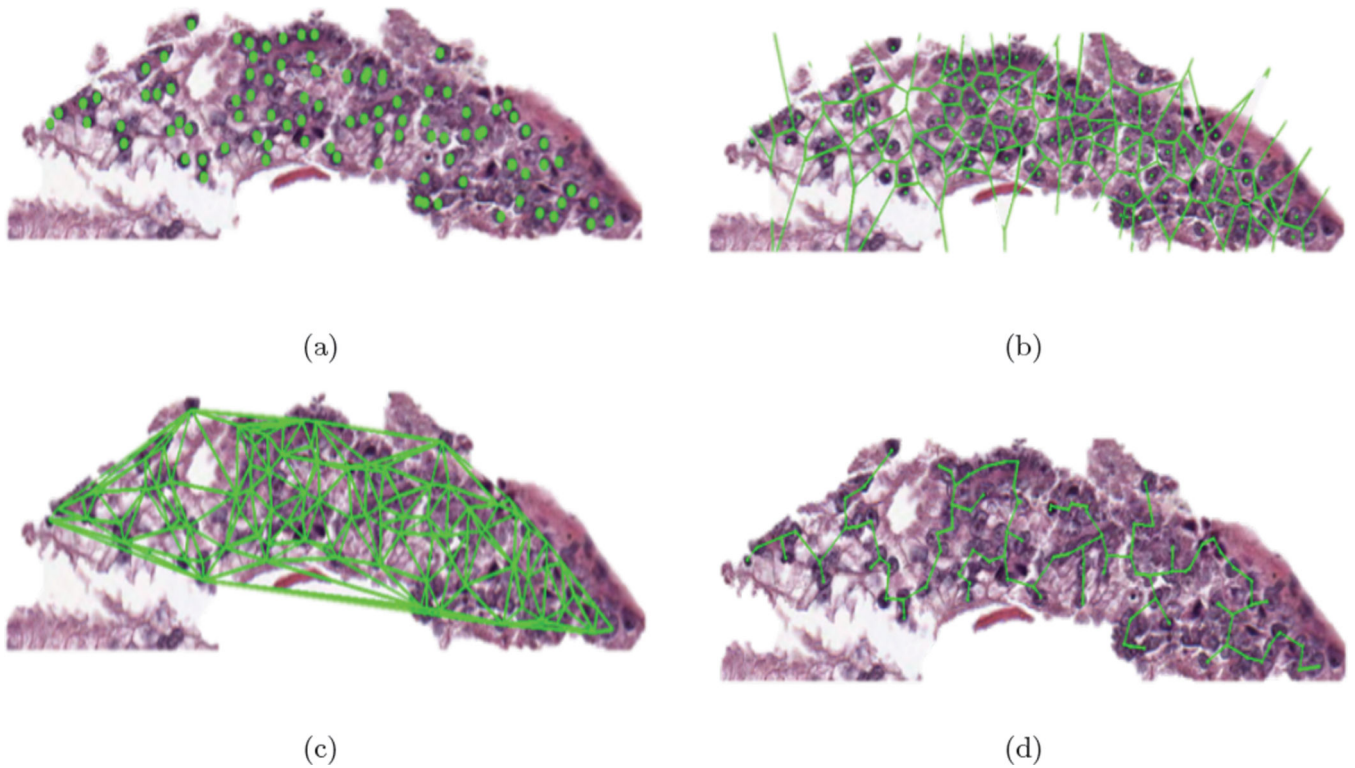


Figure 4.

Different graph features are used to model nuclear architecture of Grade 6 CaP. Shown from left to right (a) original histology image with detected nuclear centroids, (b) Voronoi diagram, (c) Delaunay triangulation, and (d) Minimum spanning tree. Nuclear centroids were used as graph vertices.

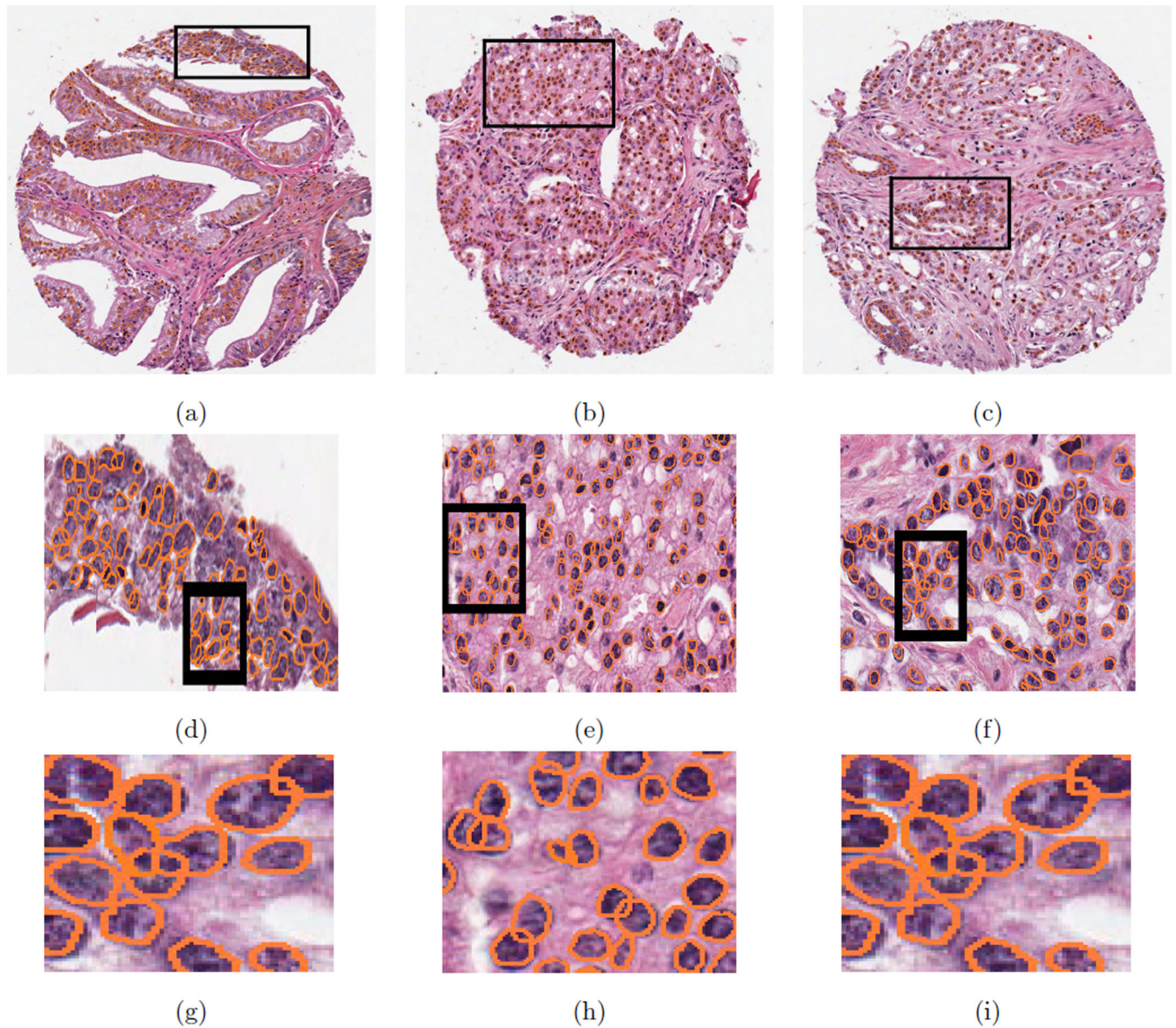


Figure 5.

(a)–(c) Nuclear segmentations (orange boundaries) for three different TMA cylinders corresponding to Gleason scores 6, 7 and 9. (b)–(f) Magnified ROI's from (a)–(c), respectively, reveal that our hybrid ACM (AdACM) with a selective shape prior is able to accurately segment almost all nuclei. (g)–(i) Further magnification of the region of interest (ROI) shown in (a), (b), (c) reveals that our model is able to accurately resolve overlaps and intersections.

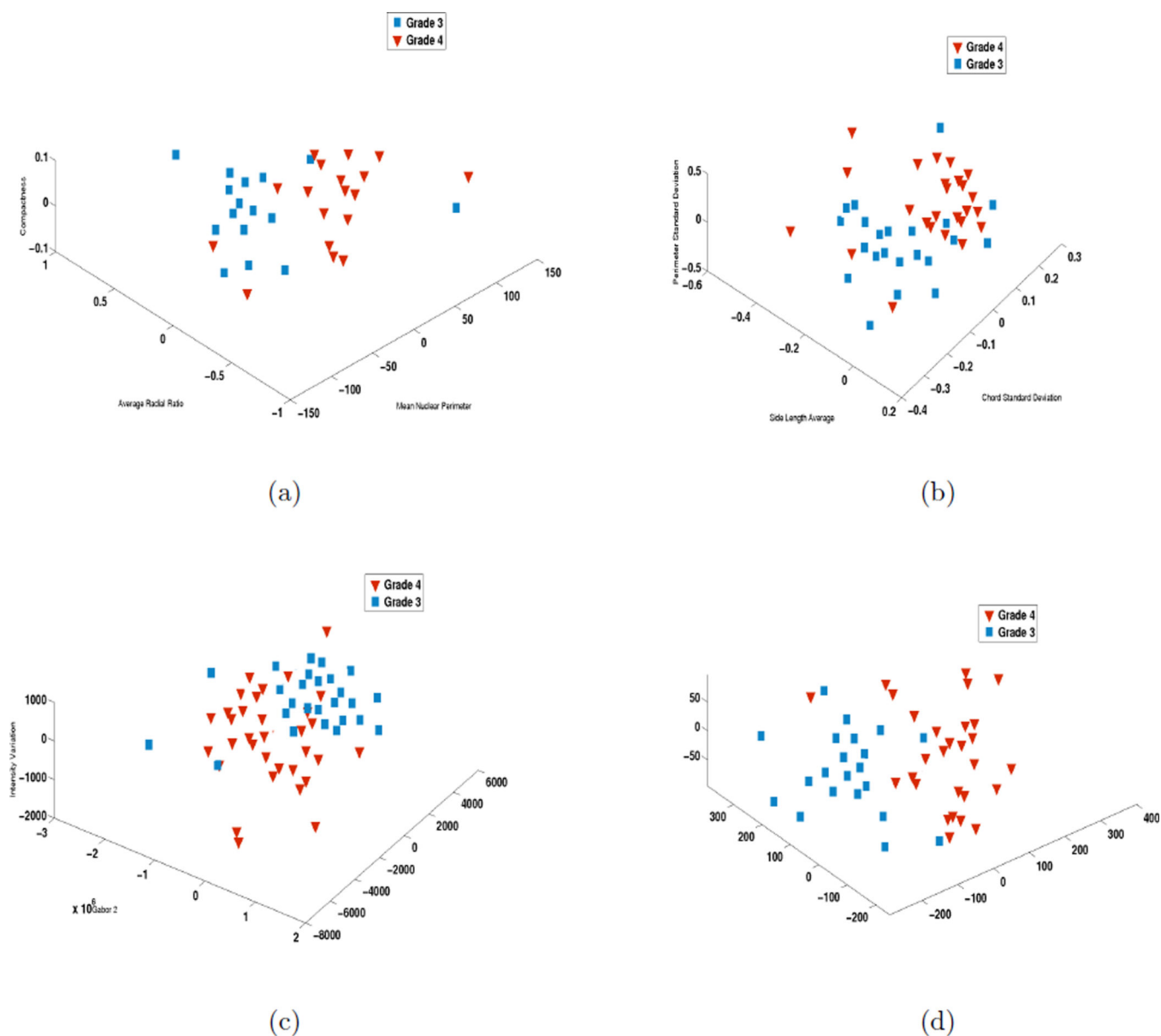


Figure 6. 3D feature plots, constructed by taking top 3 features, reveal separation of primary grade 3 and grade 4 by using (a) Nuclear (b) Textural (c) Graph based features, and (d) top 3 features given by mRMR scheme.

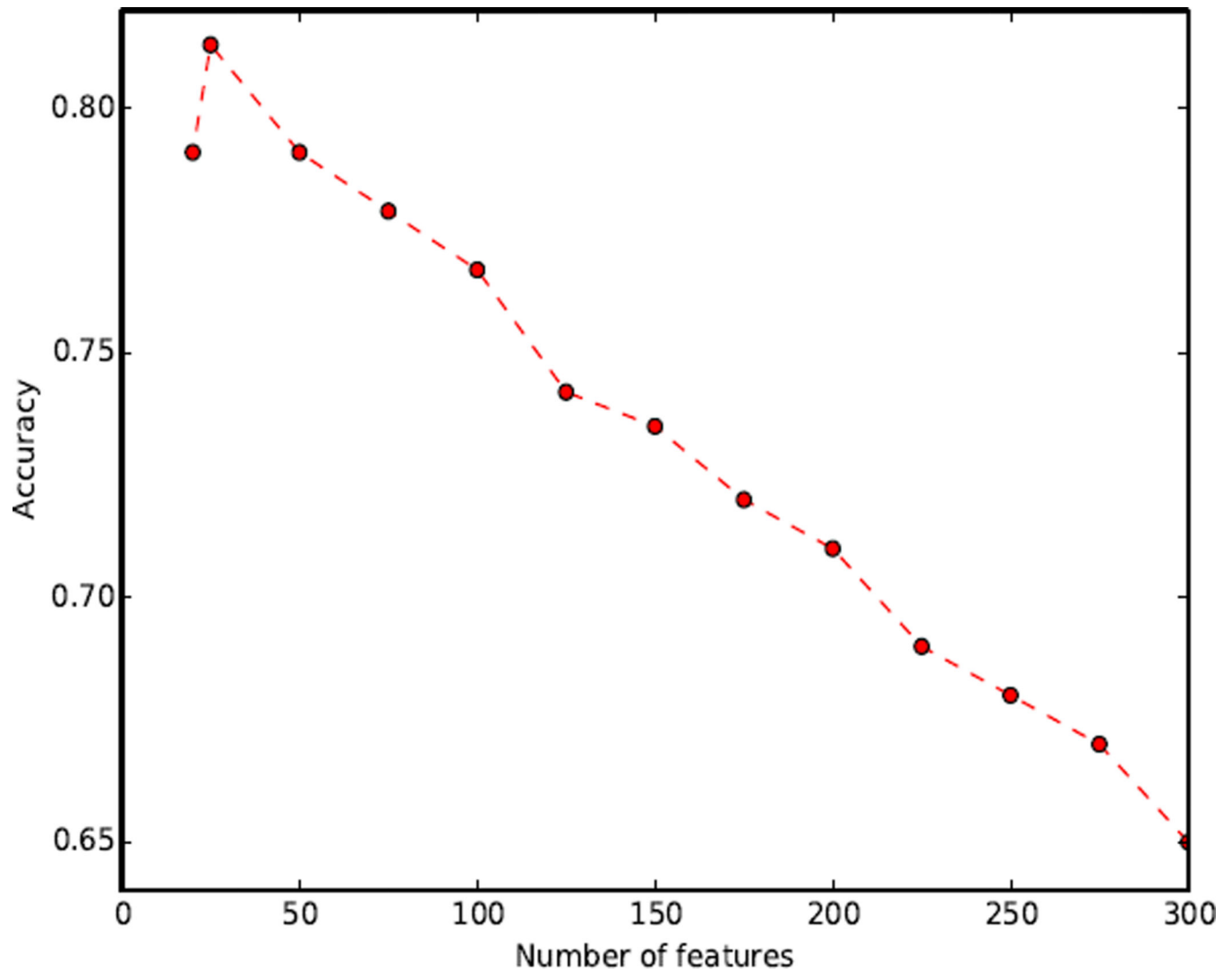


Figure 7. Plot of classifier accuracy as a function of the number of features in the ensemble. The highest classification accuracy is obtained when the number of features in the ensemble is between 25–40.

Table 1

Description of notations and commonly used symbols in this paper.

Symbol	Description	Symbol	Description
\mathcal{C}	2D image scene	\mathbf{x}	2D Cartesian grid of pixels $c = (x, y)$
$f_g(c)$	function that assigns intensity values to pixel c	s	the shape contour (zero level set)
c_w	point on contour boundary	Ω	bounded open set in \mathbb{R}^2
$H(\phi)$	Heavside function $H(\phi) = \begin{cases} 1, & \phi(c) \geq 0; \\ 0, & \phi(c) < 0. \end{cases}$	$\delta(\phi)$	Delta function $\delta(\phi) = \begin{cases} +\infty, & \phi(c)=0; \\ 0, & \phi(c) \neq 0. \end{cases}$
Ω_f	foreground region $\Omega_f = \{c \in \Omega : \phi(c) > 0\}$	Ω_b	background region $\Omega_b = \{c \in \Omega : \phi(c) < 0\}$
$\phi(c)$	the level set function	$\mathcal{A}(\cdot)$	the set of pixels within boundary
ψ	the shape function	u_{in}, u_{out}	partitioned foreground and background regions
\mathbf{F}	feature set	\mathcal{Q}	selected subset of feature set

Table 2

Summary of image derived features used to characterize architectural arrangement and morphological appearance of CaP nuclei. Relationship of graph, morphological features to visual attributes is also shown.

Feature Class	Extracted Features	Relevance to Histology
Voronoi Tessellation	Area Standard Deviation, Area Average, Area Minimum / Maximum Area Disorder, Perimeter Standard Deviation, Perimeter Average, Perimeter Minimum / Maximum, Perimeter Disorder, Chord Standard Deviation, Chord Average, Chord Minimum / Maximum, Chord Disorder	Tissue Architecture
Delaunay Triangulation	Side Length Minimum / Maximum, Side Length Standard Deviation, Side Length Average, Side Length Disorder, Triangle Area Minimum / Maximum, Triangle Area Standard Deviation, Triangle Area Average, Triangle Area Disorder	
Minimum Spanning Tree	MST Edge Length Average, MST Edge Length Standard Deviation, MST Edge Length Minimum / Maximum, MST Edge Length Disorder	
Nuclear Morphology	Area Overlap Ratio, Average Radial Ratio, Compactness, Convexity, Mean Nuclear Area, Mean Nuclear Perimeter, Mean Nuclear Diameter.	Nuclear size, boundary, appearance

Table 3

Quantitative evaluation of detection results for the 3 models over 80 prostate histology images.

	SN	PPV	OR
GAC	0.30	0.58	0.022
Rousson	0.69	0.53	0.76
Our Model	0.85	0.66	0.90

Table 4

Quantitative evaluation of segmentation, and Overlap Resolution between the Geodesic Active Contour (Caselles et al., 1997), Rousson-Deriche (Rousson and Paragios, 2002) and AdACM for 8040 randomly selected nuclei across the 80 TMA images.

	SN_a	SP_a	PPV_a	OV	HD	MAD
GAC	0.38	0.92	0.20	0.17	11.3	7.1
Rousson	0.75	0.89	0.53	0.49	2.9	1.5
Our model	0.82	1.0	0.88	0.72	2.3	0.9

Table 5

Quantitative evaluation of segmentation, and Overlap Resolution between the Geodesic Active Contour (Caselles et al., 1997), Rousson-Derliche (Rousson and Paragios, 2002) and AdACM for randomly selected nuclei across the 100 patches of 200×200 across 80 TMA images.

	Watershed/Preprocessing	Concavity Detection	Initialization	Energy Evolution
Runtime (seconds)	25	45	5	175

Table 6

Top 10 ranked features

	Feature Name	Feature Type
1	Average Radial Ratio	Nuclear
2	Perimeter Standard Deviation	Voronoi
3	Mean Nuclear Perimeter	Nuclear
4	Intensity Variation	Harlick
5	Side Length Average	Delaunay
6	Area Overlap Ration	Nuclear
7	Chord Standard Deviation	Voronoi
8	$\theta = \frac{\pi}{6}$, window: 5×5	Gabor
9	MST Edge Length Standard Deviation	Minimum Spanning Tree
10	Compactness	Nuclear

Table 7

Comparison of three methods (GAC, RD and AdACM) in predicting primary grade 3 vs 4

	GAC	RD	AdACM
Accuracy	68.8 ± 1.3%	75.1 ± 0.8%	86.1 ± 0.5%

Table 8

Classification accuracies of AdACM compared against varying feature set sizes

	QDA Accuracy
Optimal Feature Set (28)	$86.1 \pm 0.5\%$
Nuclear Features	$81.2 \pm 0.4\%$
Architectural Features	$78.7 \pm 0.6\%$
Textural Features	$68.3 \pm 0.5\%$